Materials & Design 211 (2021) 110136

Contents lists available at ScienceDirect

Materials & Design

journal homepage: www.elsevier.com/locate/matdes

Influence of the non-metal species on the oxidation kinetics of Hf, HfN, HfC, and HfB_2 coatings

T. Glechner [a,*], O.E. Hudak [a], T. Wojcik [a], L. Haager [b], F. Bohrn [b], H. Hutter [b], O. Hunold [c], J. Ramm [c], S. Kolozsvári [d], E. Pitthan [e], D. Primetzhofer [e], H. Riedl [a,f]

[a] Christian Doppler Laboratory for Surface Engineering of High-performance Components, TU Wien, Austria
[b] Institute of Chemical Technologies and Analytics, TU Wien, A-1060 Wien, Austria
[c] Oerlikon Balzers, Oerlikon Surface Solutions AG, LI-9496 Balzers, Liechtenstein
[d] Plansee Composite Materials GmbH, D-86983 Lechbruck am See, Germany
[e] Department of Physics and Astronomy, Uppsala University, SE-75120 Uppsala, Sweden
[f] Institute of Materials Science and Technology, TU Wien, A-1060 Wien, Austria

HIGHLIGHTS

- Broad variation of oxidation kinetics for Hf, $HfC_{0.96}$, $HfN_{1.5}$ and $HfB_{2.3}$ coatings.
- Hf, $HfC_{0.96}$, $HfN_{1.5}$ and $HfB_{2.3}$ coatings exhibit different oxide scale morphologies.
- Comparable oxidation resistance of $HfN_{1.5}$ and $HfB_{2.3}$ coatings.
- Exceptional low oxygen inward diffusion for $HfB_{2.3}$ coatings at 900 °C.
- Study highlights the impact of the non-metal species on the oxidation resistance.

GRAPHICAL ABSTRACT

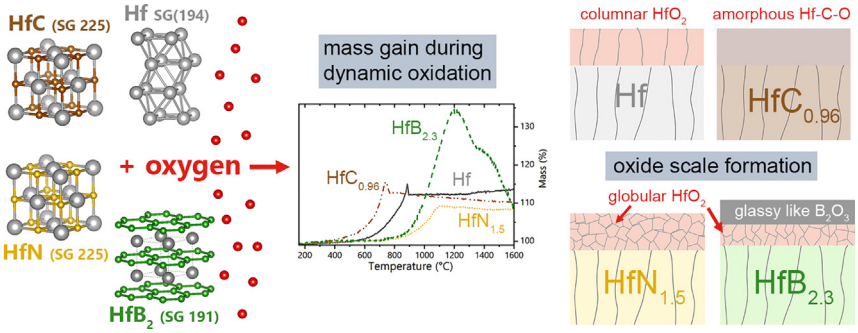

ARTICLE INFO

Article history:
Received 7 July 2021
Revised 27 August 2021
Accepted 27 September 2021
Available online 28 September 2021

Keywords:
Thin films
Borides
Oxide-film growth kinetics
Oxidation
Hafnium

ABSTRACT

The influence of the non-metal species on the oxidation resistance of transition metal ceramic based thin films is still unclear. For this purpose, we thoroughly investigated the oxide scale formation of a metal (Hf), carbide ($HfC_{0.96}$), nitride ($HfN_{1.5}$), and boride ($HfB_{2.3}$) coating grown by physical vapor deposition. The non-metal species decisively affect the onset temperature of oxidation, ranging between 550 °C for $HfC_{0.96}$ to 840 °C for $HfN_{1.5}$. $HfB_{2.3}$ and $HfN_{1.5}$ obtain the slowest oxide scale kinetic following a parabolic law with k_p values of $4.97 \cdot 10^{-10}$ and $5.66 \cdot 10^{-11}$ $kg^2\ m^{-4}\ s^{-1}$ at 840 °C, respectively. A characteristic feature for the oxide scale on Hf coatings, is a columnar morphology and a substantial oxygen inward diffusion. $HfC_{0.96}$ reveals an ineffective oxycarbide based scale, whereas $HfN_{1.5}$ features a scale with globular HfO_2 grains. $HfB_{2.3}$ exhibits a layered scale with a porous boron rich region on top, followed by a highly dense and crystalline HfO_2 beneath. Furthermore, $HfB_{2.3}$ presents a hardness of 47.7 ± 2.7 GPa next to an exceptional low inward diffusion of oxygen during oxidation. This study showcases the strong influence of the non-metallic bonding partner despite the same metallic basis, as well as the huge potential for HfB_2 based coatings also for oxidative environments.

* Corresponding author.
E-mail address: thomas.glechner@tuwien.ac.at (T. Glechner).

https://doi.org/10.1016/j.matdes.2021.110136
0264-1275/

1. Introduction

Surface protection of highly stressed components used in aviation and energy industries is a highly relevant topic with respect to sustainable development and extending the longevity of high-end machine elements. Such applications demand for materials that can endure extremely harsh environments, including highest temperatures, diverse chemical strain, as well as wear and erosion exposures [1,2]. In order to access new temperature regimes [3] novel coating concepts, as well as their deposition techniques are needed. Here, physical vapor deposition (PVD) constitutes a key technology, as the design capabilities for new thin film materials are nearly unlimited.

For the development of coatings protecting underlying components against oxidation at high temperatures, two different strategies can be distinguished: *(i)* direct deposition of an oxide e.g. Al-Cr-O [4], or *(ii)* thermo-chemical oxidation of a deposited coating, rendering a protective oxide scale, i.e. through strong oxide formers [5]. For the second approach the group of Ultra High Temperature Ceramics (UHTC) comes into focus when striving for very high operation temperatures. This material group mainly comprises carbides, borides, and nitrides of group IV to VI transition metals (TM). Whereas a lot of studies have been done on oxidation resistant UHTC boride and carbide based bulk ceramics [6–8], the development of protective PVD coatings has mainly focused on TM-nitrides, (TiN, $Ti_{1-x}A_xlN$, CrN [9]). To improve the rather poor oxidation resistance of nitride coatings, various alloying concepts have been employed in the field of hard coatings. These concepts concentrated on alloying strategies for the metal sublattice e.g. replacing Ti with Al in $Ti_{1-x}Al_xN$ or adding additional metals e.g. $Ti_{1-x-y}Al_xTa_yN$ to form highly dense and adherent scales [10–12]. However, the adaptation of the non-metallic bonding partner – in particular nitrogen – to enhance the oxidation resistance, was not into the focus as nitrogen does not interact with oxygen and simply gets released during oxidation. Different studies examined the effect of the stoichiometry [13,14] on the phase stability and related mechanical properties, or the addition of further elements, e.g. fluorine [15]. Nevertheless, for the design of novel oxidation resistant coating materials in the field of UHTCs, non-metallic species such as carbon and boron need to be considered as they react with oxygen, forming CO/CO_2 and B_2O_3, respectively. Understanding the role of these species during oxidation is therefore crucial for developing strategies to improve the oxidation resistance of TM boride and carbide based coatings [16–19].

Therefore, this study compares metal, carbide, boride, and nitride coatings, which all exhibit the same metal oxide former, hafnium, in order to evaluate the role of the non-metal species during oxidation. Hafnium was chosen due to the extremely high thermal stability of HfB_2, HfC, HfN, and in particular HfO_2 (T_m = 2810 °C [20]). This property makes hafnium based thin films very promising for high temperature applications. Furthermore, HfB_2 is considered to exhibit the highest oxidation resistance among transition metal diborides [8].

2. Experimental details

All hafnium based thin films were deposited using an in-house built magnetron sputter deposition system (so-called FRIDA). Three different round 3-inch targets were used: metallic hafnium, HfB_2 and HfC (Plansee Composite Materials GmbH). The targets were sputtered in a pure argon atmosphere in order to obtain the metallic hafnium, HfB_{2-z} and HfC_x coatings. For HfN_y, the hafnium target was operated in an argon/nitrogen mixture (28% nitrogen of the total gas flow). A flow controlled working pressure of 0.57 Pa was chosen for all depositions, corresponding to a total flow rate of 32 sccm. For all depositions, the target and substrate holder were aligned parallel at a distance of 73 mm with an applied bias potential of −70 V. To provide similar homologous temperatures (T/T_m) across all material systems during deposition, 350, 550, and 600 °C were chosen for Hf, HfN and HfB_2, and HfC, respectively. All targets were operated in DC mode with a target current of 0.55 A (except for HfC, where a lower target current of 0.4 A was used in order to reduce residual stresses achieving proper film adhesion).

All thin films were deposited on as fired polycrystalline (20x7x0.38 mm^3) and single crystalline (10x10x0.53 mm^3) Al_2O_3 substrates. Due to the higher surface roughness of the polycrystalline samples, ToF-SIMS and TEM analysis were only conducted on the single crystalline substrates. Before deposition, each substrate-surface was freed from impurities in an ultrasonic bath using ethanol and acetone. Furthermore, the targets and the substrates were sputter-cleaned in a pure argon atmosphere immediately before deposition.

To determine the structure of the thin films, X-ray diffraction (XRD) in Bragg Brentano configuration was done, utilizing a Panalytical Empyrean diffractometer equipped with a Cu-Kα radiation source (wavelength λ = 1.5418 Å). The mechanical properties, such as hardness and Young's modulus, were determined by nanoindentation using an Ultra-Micro-Indentation System (UMIS) equipped with a Berkovich diamond tip. For every sample, 30 idents with different applied loads (3 to 45 mN) were performed to subsequently evaluate the load–displacement curves after Oliver and Pharr [27]. For the calculation of the Young's modulus, Poisson ratios were taken from Ref. [16,21,22]. To study the structure and morphology of the formed oxide scale and the remaining thin film a scanning electron microscope (SEM, FEI Quanta 250 FEGSEM operated at 5 keV) and a Transmission Electron Microscope (TEM, FEI TECNAI F20, equipped with a field emission gun and operated at an accelerating voltage of 200 kV) were used. The samples were prepared for TEM by mechanical polishing using a decreasing grinding paper grain size. The samples were further thinned using a PIPS (Precision ion polishing system, Gatan inc.) in low-voltage-mode to increase TEM transparency.

Oxide growth kinetics, were determined using a combined differential scanning calorimetry (DSC)/thermo-gravimetric analysis (TGA) system, which was equipped with a Rhodium furnace (Netzsch STA 449 F1). The limit of the TGA where significant effects can be detected is 10 μg. The substrates were weighed before and after deposition with an analytical balance (Radwag AS 82/220.R2) to determine the thin film weight. For each measurement a baseline measurement with empty crucibles was carried out. The coated substrate was then placed into the crucible and heated up under a flowing gas stream. Prior to all oxidation treatments, all samples were thermally cleaned (for 20 min) within the DSC/TG system at 110 °C in pure Helium atmosphere. Dynamic oxidation was performed at a heating rate of 10 K/min up to 1600 °C in synthetic air (50 ml/min). For isothermal oxidation the sample was preheated up to the desired temperature in a pure helium atmosphere with 20 K/min and then isothermally oxidized in synthetic air (50 ml/min). In both cases, cooling down was carried out with 25 K/min in pure Helium, respectively. In order to protect the scales of the Netzsch STA 449 F1 an additional Helium flow of 20 ml/min was passed through the furnace.

For determining the chemical composition and total areal densities of the coatings, Time-of-flight Elastic Recoil Detection Analysis (ERDA) and elastic backscattering spectroscopy (EBS) were employed at the tandem accelerator laboratory of Uppsala University. For ToF-ERDA, measurements were performed using a 44 MeV I^{10+} primary ion beam and detecting recoils at a detection angle of 45° by a segmented gas ionization chamber [23]. EBS was carried out with a detection angle of 170° using 4.35 MeV $^4He^+$ ions to

obtain the total areal densities of the films and use the strong ^{12}C (^{4}He,^{4}He)^{12}C elastic resonance at ~ 4.260 MeV [24]. The relative uncertainty of the chemical compositions deduced from the combination of both techniques considering both systematic and statistical uncertainties is around 5%.

The elemental distribution over depth in the oxidized states was studied using Time of Flight Secondary Ion Mass Spectrometry (ToF-SIMS). The ION TOF.SIMS 5 system (IONTOF GmbH) was operated with two beams using Bi^{1+} ions (acceleration voltage 25 keV) as the primary ion species, and Cs^{+} (acceleration voltage 2 keV) for the crater erosion, in order to detect electronegative elements, such as oxygen. All samples were measured in the High Current Bunch Mode (HCBU) with interlaced measurement setting, to obtain depth profiles with high mass resolution. Scanning of the surface was set to sawtooth, capturing 128 × 128 pixels with a field of view of 100 μm × 100 μm and a crater size of 300 μm × 300 μm.

3. Results and discussion

As illustrated in Fig. 1, different Hf-based compounds form various crystal structures. Metallic Hf exhibits a hexagonal structure (SG 194) at room temperature, whereas HfC and HfN are stabilized in a fcc-rock salt structure (SG 225) with the non-metal atoms located in the octahedral sites. HfB_2 forms a hexagonal structure (SG 191, also referred to as α-HfB_2) where the metal and non-metal atoms are arranged in layers. Exposing these compounds to oxygen containing atmospheres, different reactions occur, namely:

$$Hf + O_2 \rightarrow HfO_2 \quad (1)$$

$$HfC + 3/2\ O_2 \rightarrow HfO_2 + CO \quad (2)$$

$$HfC + 2\ O_2 \rightarrow HfO_2 + CO_2 \quad (3)$$

$$2\ HfN + 2\ O_2 \rightarrow 2\ HfO_2 + N_2 \quad (4)$$

$$HfB_2 + 5/2\ O_2 \rightarrow HfO_2 + B_2O_3 \quad (5)$$

In general, hafnium oxidizes to HfO_2, which can be stabilized in different polymorphs: monoclinic (m), tetragonal (t), and cubic (c), respectively. The *ortho*-rhombic phase is also observed at high pressure conditions [25]. While m-HfO_2 (SG 14) is stable in ambient conditions, the oxide undergoes a transition to t-HfO_2 at 1820 °C and finally to c-HfO_2 at 2505 °C [26]. Whereas boron and carbon (originating from HfB_2 and HfC) oxidize to B_2O_3 (T_{melt} = 450 °C [27]) and gaseous CO and/or CO_2, respectively, nitrogen does not interact with oxygen, and is simply released as N_2. Hence, out of all oxidation products, solely HfO_2 and B_2O_3 are capable of forming an adherent and protective oxide scale.

The chemical analysis of the deposited thin films done by ERDA and EBS indicate that the metallic hafnium and the HfC target contain a certain amount of Zr, which leads to a Zr content of around 7 at.% in the metal coating, 3.5 at.% in the nitride based coating and 1.5 at.% in the carbide coating. For simplicity purposes and due to the fact that Zr chemically resembles Hf, the Zr and Hf content are summed up in the notations. Around 3.9 at.% of oxygen was observed by ToF-ERDA in the carbide based coating while the other coatings presented less than 0.2 at.%. Further, details on the compositions of the coatings can be found in Table A1 in the Appendix. The contents of the non-metal species (taking the mean value between ERDA and EBS) are 70.1 at.% boron, 60.0 at.% nitrogen and 47.2 at.% carbon for the corresponding boride, nitride, and carbide coating, respectively. Therefore, the notations of the coatings are $HfN_{1.5}$, $HfC_{0.96}$ and $HfB_{2.3}$, considering only the non-metal to Hf ratio (e.g. $HfC_{0.96}$ = (C = 47.15)/(Hf + Zr = 48.90)). The densities of the coatings determined using the total areal densities obtained by EBS and the coating thicknesses obtained by SEM were 12.4, 11.2, 12.2, and 8.9 g/cm^3 for Hf, $HfC_{0.96}$, $HfN_{1.5}$ and $HfB_{2.3}$, respectively, which are slightly lower than the nominal densities reported for the perfectly stoichiometric compounds in Ref. [28] being 13.3, 12.2, 13.8 and 10.5 g/cm^3. The Hf coatings exhibit a moderate hardness of 7.2 ± 0.24 GPa (Young's modulus: 214 ± 15 GPa), whereas $HfN_{1.5}$ and $HfC_{0.96}$ feature high hardness of 31.5 ± 1.8 GPa and 32.6 ± 1.8 GPa, respectively (Young's modulus: 417 ± 26 GPa and 431 ± 19 GPa, respectively). Above all, $HfB_{2.3}$ coatings exhibit a superior hardness of 47.7 ± 2.7 GPa with a Young's modulus of 612 ± 25 GPa. Nevertheless, these results indicate for all coating materials a rather dense and solid morphology.

The diffractograms presented in Fig. 2 feature the as-deposited crystal structure (top pattern in each sub-figure) as well as the evolution due to oxidation (Hf - T_{Ox} = 640 °C for 1 h, $HfC_{0.96}$ - T_{Ox} = 550 °C for 1 h, $HfN_{1.5}$ - T_{Ox} = 840 °C for 1 h, and $HfB_{2.3}$ - T_{Ox} = 900 °C for 30 min). To analysis the phase formation due to oxygen, the oxidation treatments were chosen in that way to allow a remaining unaffected coating next to the formed scale. In the as-deposited state, all thin films appear single phased, forming the expected crystal structures as shown in Fig. 1. The face-centered cubic $HfN_{1.5}$ exhibits a strong (200) texture and a shift to lower 2 theta

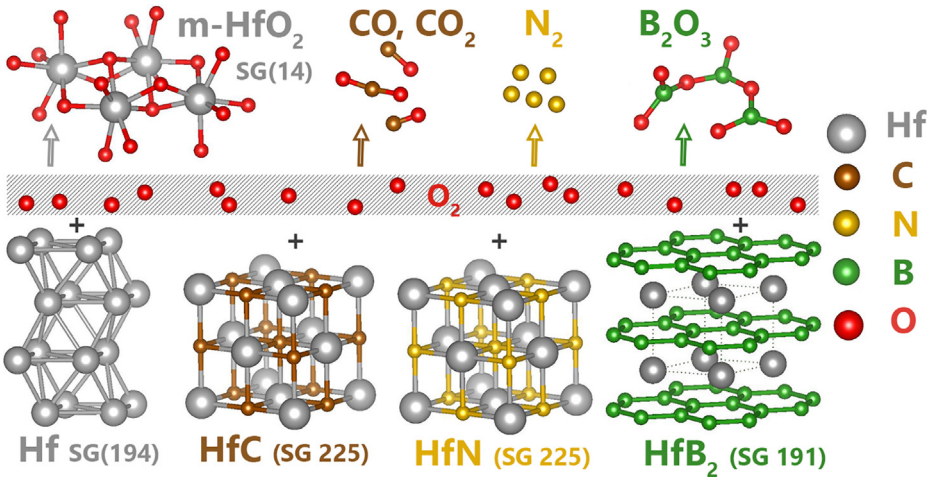

Fig. 1. Schematic of the various oxidation products that will occur when exposing Hf, HfC, HfN and HfB_2 to oxygen.

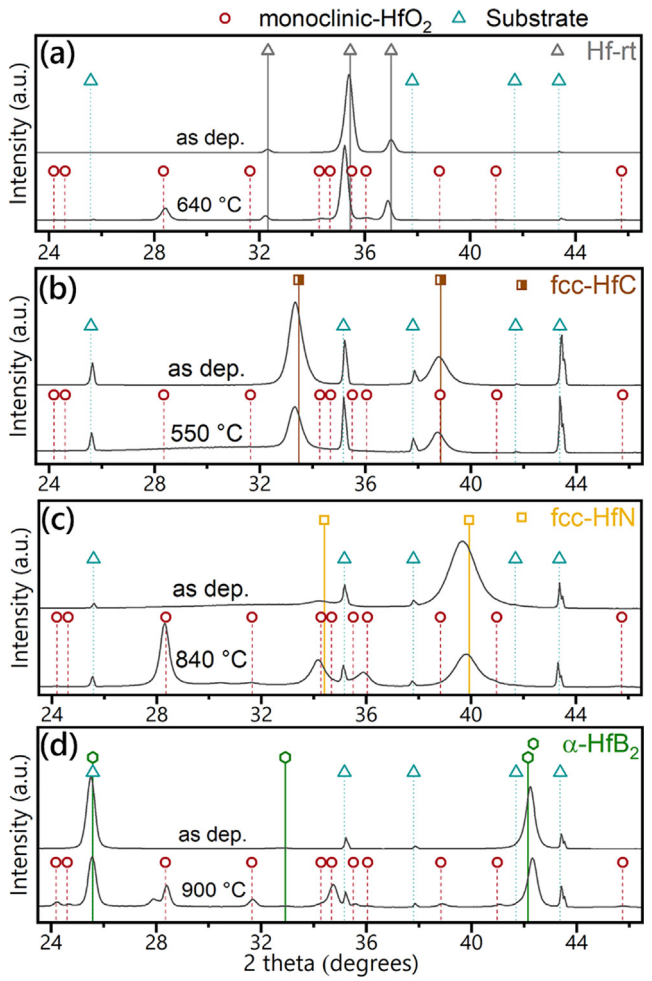

Fig. 2. XRD analysis of the Hf based coatings in as deposited state (upper spectra) and in a representative oxidized state. (a) Hf coating as dep. and oxidized at 640 °C (Hf-rt [41]), (b) $HfC_{0.96}$ coating as dep. and oxidized at 550 °C (HfC [42]), (c) $HfN_{1.5}$ coating as dep. and oxidized at 840 °C (HfN [43]) and (d) $HfB_{2.3}$ coating as dep. and oxidized at 900 °C (α-HfB_2 [44]). The reference patterns for monoclinic HfO_2 and Al_2O_3 substrate were taken from [45] and [46] respectively.

diffraction angles, suggesting the presence of high compressive stresses. On the other hand, fcc-$HfC_{0.96}$ and α-$HfB_{2.3}$ display a slight texture in (111) and (001) orientation, respectively. After oxidation, monoclinic HfO_2 is formed for all compounds except $HfC_{0.96}$. For $HfC_{0.96}$ at T_{Ox} = 550 °C only a broad hump is visible in the oxidized state, pointing towards an amorphous scale – the same was observed for 500 and 600 °C. In addition, no signs of crystalline B_2O_3 could be made out for the oxidized $HfB_{2.3}$. The as deposited coatings exhibit a thickness of around 2 μm, except for $HfC_{0.96}$ obtaining a reduced thickness of 1 μm due to residual stresses and adhesion problems when deposited onto Al_2O_3 substrates.

Dynamic oxidation of the thin films reveals large differences between the various Hf based compounds (Fig. 3a). For all measurements the mass signal stays constant up to a certain temperature and then rises due to the growth of the oxide scale (small drifts are of course noticeable, being related to minor differences between the measurement and respective calibration run). The onset temperature of this rise will be referred to as oxidation onset temperature. It is 550 °C for $HfC_{0.96}$, 640 °C for Hf, 800 °C for $HfB_{2.3}$ and 840 °C for $HfN_{1.5}$. This temperature was determined as the intersection of a tangent in the temperature regime with no mass change and a tangent for the initial increasing mass. Interestingly enough, Hf, HfC, and HfN show quite a large difference of the oxidation onset temperature even though all these coatings rely solely on HfO_2 for oxidation protection. This suggests that the non-metal species possess quite a large influence on the oxide scale formation. At a certain temperature the coatings are completely oxidized and the mass gain settles at a specific value – i.e. 700 °C for $HfC_{0.96}$ or 1100 °C for $HfN_{1.5}$. For Hf, a steep mass decrease was observed after this temperature, being attributed to the spallation of parts of the scale– see full grey line in Fig. 3a. $HfC_{0.96}$ exhibits a similar TG trend, however with no observable spallation of the scale. S. Shimada [29] reports a very similar TG curve when oxidizing HfC powder. With additional mass spectrometry measurements, he showed that first a considerable amount of carbon stays unoxidized within the sample, which is then oxidized and released as CO or CO_2 and forms this peak. With an additional mass decrease measured for $HfC_{0.96}$, it is presumed that small amounts of carbon remain within the scale, being subsequently oxidized and released with increasing temperature – see brown dash dotted line in Fig. 3a. The behavior for $HfB_{2.3}$ is considerably different, where after a peak at 1200 °C, the mass continuously decreases down to 1600 °C. This can be attributed to an evaporation of the liquid boron oxide [30,31]. The nominal mass increase after equations 1–5 for the stoichiometric compounds would be 118 % for Hf, 110 % for HfC, 109 % for HfN, 140 % for HfB_2 including B_2O_3 and 105 % excluding B_2O_3. The experimentally obtained weight gains of the coatings after dynamic oxidation up to 1600 °C are 114 % for Hf, 110.2 % for $HfC_{0.96}$, 108.5 % for $HfN_{1.5}$ and 108.6 % $HfB_{2.3}$. This fits very well to the theoretical values when taking the spallation for the Hf coating into account. Furthermore, also the mass decrease from 134.5 to 108.6 % for $HfB_{2.3}$ is in excellent agreement considering the evaporation of B_2O_3.

In addition to the dynamic oxidation, isothermal oxidation treatments were performed in order to determine the oxide growth kinetics of the Hf-based compounds – again using coatings deposited on hard Al_2O_3 substrates (20x7 mm^2). At least three temperatures were chosen for each system, one at the oxidation onset temperature, one 100 °C below and another one 100 °C above. For $HfC_{0.96}$ an interval of only 50 °C was chosen, due to the rapidly progressing oxidation process. Furthermore, we added an additional temperature for $HfN_{1.5}$ and $HfB_{2.3}$ to improve the fit quality in the Arrhenius plot. Moreover, the holding temperature was shortened with increasing temperature (see Fig. 3b to e), in order to avoid thick oxide scales that in turn would have made the SIMS analysis more difficult, due to high local charging of the surface. For all coating materials, we obtained parabolic growth kinetics (Equation (6)) with an increasing rate constant k_p with rising temperatures (see Fig. 3b to e). Hence, the diffusion through the oxide scale is the rate determining step.

$$\left(\frac{\Delta m}{A}\right)^2 = k_p \cdot t \tag{6}$$

$$k_p = k_0 \cdot e^{-\frac{E_a}{RT}} \tag{7}$$

In Equation (6) and (7) Δm is the mass gain due to oxidation, A the area which is oxidized, k_p the parabolic rate constant, t the time, k_0 the parabolic rate pre-exponential factor, E_a the activation energy, R the universal gas constant and T the temperature. To compare and discuss the different reaction kinetics of the formed oxide scales, we determined the k_p values (Table 1) and plotted them in an Arrhenius plot (see Fig. 4). The k_p-values are defined by the slope of the linear fit of $(\Delta m/A)^2$ (not included in the manuscript). However, $HfC_{0.96}$ is drastically oxidized at 600 °C and tends to grow almost linearly at this temperature – see evolution for 600 °C in Fig. 3c. Based on this behavior, we did not include the data point in Fig. 4.

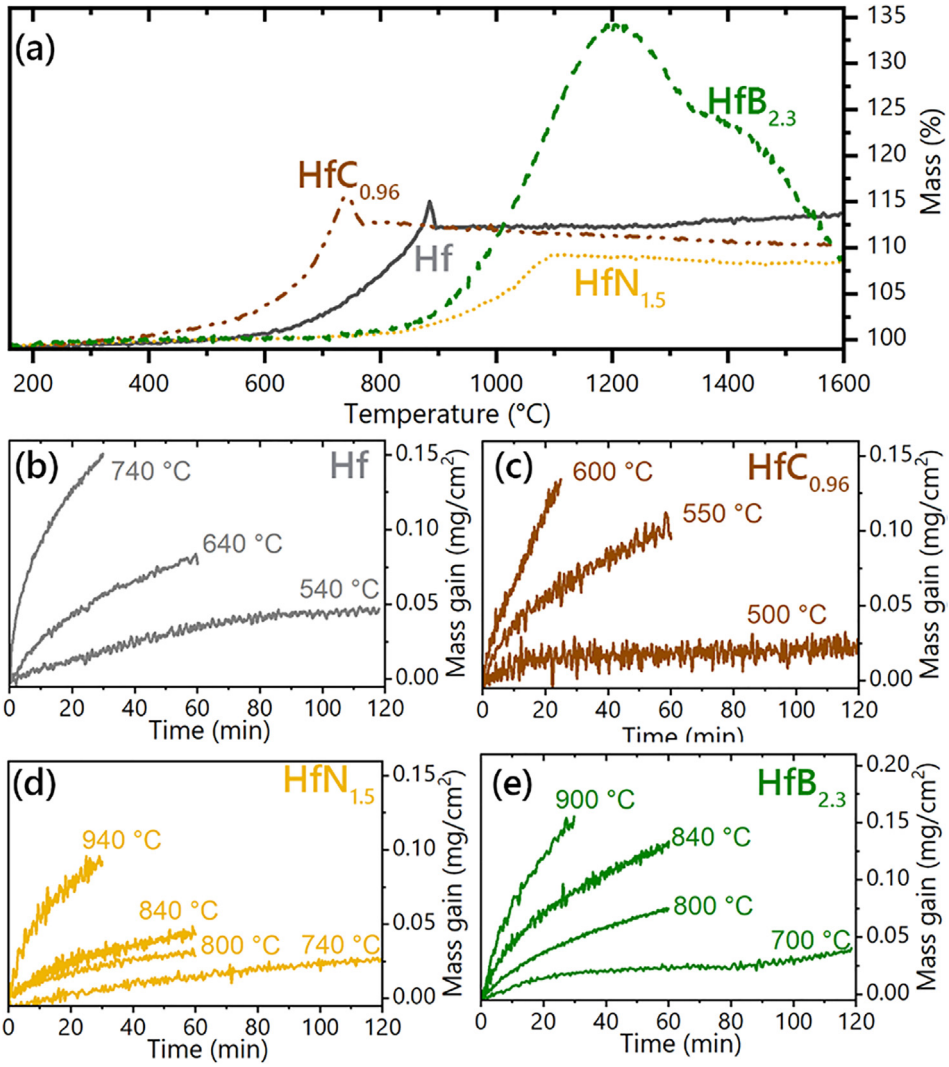

Fig. 3. Dynamic oxidation of the hafnium based thin films on hard Al_2O_3 substrates in synthetic air up to 1600 °C at a heating rate of 10 K/min (a). Mass gain per area during isothermal oxidation in synthetic air at temperatures around the oxidation onset temperature (T_{ox}) for Hf (b), $HfC_{0.96}$ (c), $HfN_{1.5}$ (d) and $HfB_{2.3}$ (e) coatings. T_{ox} of these coatings are 640 °C, 550 °C, 840 °C and 800 °C, respectively.

Table 1
Parabolic rate constants k_p determined for the different coating materials at the isothermal oxidation temperatures.

Hf		**$HfC_{0.96}$**		**$HfN_{1.5}$**		**$HfB_{2.3}$**	
E_a = 120.34 kJ				E_a = 190.21 kJ		E_a = 183.25 kJ	
k_0 = 0.00185 $kg^2\ m^{-4}s^{-1}$				k_0 = 0.119 $kg^2m^{-4}s^{-1}$		k_0 = 0.187 $kg^2\ m^{-4}\ s^{-1}$	
	k_p ($kg^2\ m^{-4}s^{-1}$)		**k_p** ($kg^2\ m^{-4}s^{-1}$)		**k_p** ($kg^2\ m^{-4}s^{-1}$)		**k_p** ($kg^2\ m^{-4}\ s^{-1}$)
540 °C	$3.63 \cdot 10^{-11}$	500 °C	$1.42 \cdot 10^{-11}$	740 °C	$1.07 \cdot 10^{-11}$	700 °C	$2.94 \cdot 10^{-11}$
640 °C	$1.99 \cdot 10^{-10}$	550 °C	$3.04 \cdot 10^{-10}$	800 °C	$2.89 \cdot 10^{-11}$	800 °C	$1.67 \cdot 10^{-10}$
740 °C	$1.25 \cdot 10^{-9}$			840 °C	$5.66 \cdot 10^{-11}$	840 °C	$4.97 \cdot 10^{-10}$
				940 °C	$4.93 \cdot 10^{-10}$	900 °C	$1.39 \cdot 10^{-9}$

For the Arrhenius plot – $\ln(k_p)$ is plotted on the y-axis versus 1/T on the x-axis – a linear dependency of $\ln(k_p)$ for $HfN_{1.5}$, $HfB_{2.3}$ and Hf is featured, indicating a direct correlation between k_p and the temperature, hence confirming no changes in the oxide growth mode. According to equation (7) the slope of the linear increase equals $-E_a/R$ and the y-axis intersection at x = 0 gives $\ln(k_0)$. The obtained values are summarized in Table 1. Based on DFT calculations presented in Ref. [16,32], the gained energy through the conversion into HfO_2 is highest for metallic Hf followed by HfC, HfB_2, and HfN. This trend is also reflected in the activation energies obtained for Hf, $HfN_{1.5}$, and $HfB_{2.3}$, where $HfN_{1.5}$ obtains the highest value and Hf the lowest – see Table 1. For $HfC_{0.96}$ the slope is even steeper compared to $HfN_{1.5}$ ($>E_a$). However, as the slope originates from only two points, its significance and validity should be considered with caution. Furthermore, XRD analysis does not suggest the formation of HfO_2 as e.g. for $HfN_{1.5}$ hence a direct comparison of E_a would also not be valid. Nevertheless, the k_p measured for Hf is in very good agreement with values from literature for the growth of HfO_2 on Hf [27]. Hence, $HfN_{1.5}$ and $HfB_{2.3}$ lead to an improvement of k_p by two orders of magnitude with respect to the oxidation temperature, placing it within a close range of e.g. Cr_2O_3 growing on Cr [27,33]. In order to ensure long time sta-

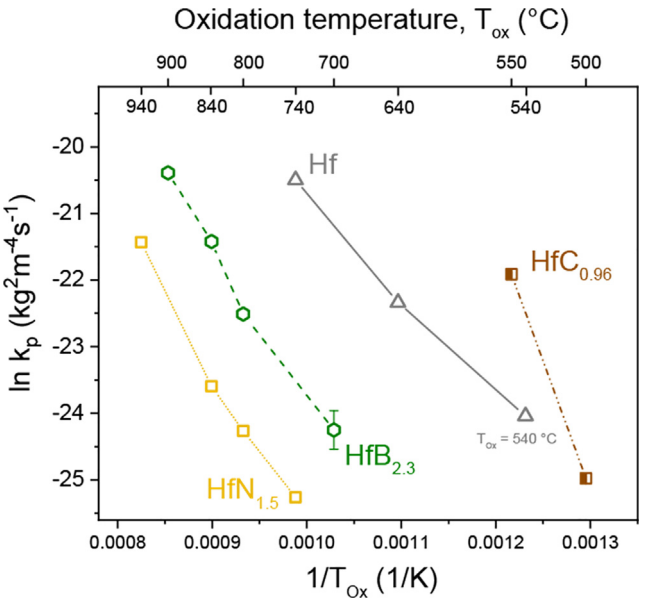

Fig. 4. Arrhenius plot of the parabolic rate constants k_p, which are calculated from the isothermal oxidation treatments shown in Fig. 3b-e.

bility of the thin films, these results suggest that the maximum operation temperature should be at least around 50 °C below the oxidation onset temperature ensuring k_p values in the range of 10^{-11} $kg^2m^{-4}s^{-1}$. Furthermore, 100 °C difference in T_{ox} corresponds to around one order of magnitude difference in the k_p-value in the Arrhenius plot. In summary, the given data strongly suggests that the kinetic of the HfO_2 formation is strongly influenced by the non-metallic bonding partner of Hf-based thin films and a more detailed consideration is necessary.

To determine the elemental distribution over the scale-coating interface, SIMS was chosen due to its high depth resolution as well as superior sensitivity for light elements, such as boron. However, depending on the material the yield of the secondary ions can vary significantly, rendering intensities of the secondary ions that do not correspond to the exact quantities. Therefore, it should be mentioned that the data shown in Figs. 5 and 6, does not represent any absolute quantification. Instead only the individual elemental trends are hereby considered and evaluated. Heavy oxygen (O^{18-} ions) was chosen for representing the oxygen content, due to the fact that O^{16-} ions are in saturation within the oxide scale, hence changes of the oxygen signal would not be distinguishably. Furthermore, the intensity of negative Hf ions is very low due to the fact that metals naturally tend to form positive ions. However, as we were more interested in the non-metal species, especially oxygen, we accepted the lower accuracy for Hf. The graphs have to be read from left to right with the surface positioned on the left-hand side and the coating-substrate interface on the right-hand side.

SIMS analysis of the oxidized Hf coatings (Fig. 5a-b) shows significant oxygen inward diffusion into the coating. For 640 °C, (Fig. 5a) oxygen has diffused through the entire coating and also increased the oxygen level of the suspected remaining metallic Hf coating. This is also clearly visible comparing the profiles at 540 and 640 °C. A similar effect has also been reported in literature for bulk Ti and Zr, which featured a high oxygen solubility [34]. Despite exhibiting a parabolic oxidation rate, the rate comprises a combination of two processes: Oxide scale growth and oxygen dissolution into the metal [35,36].

In the case of $HfC_{0.96}$, the coating oxidizes at 550 °C (Fig. 5d), but the oxygen inward diffusion occurred significantly less, with high

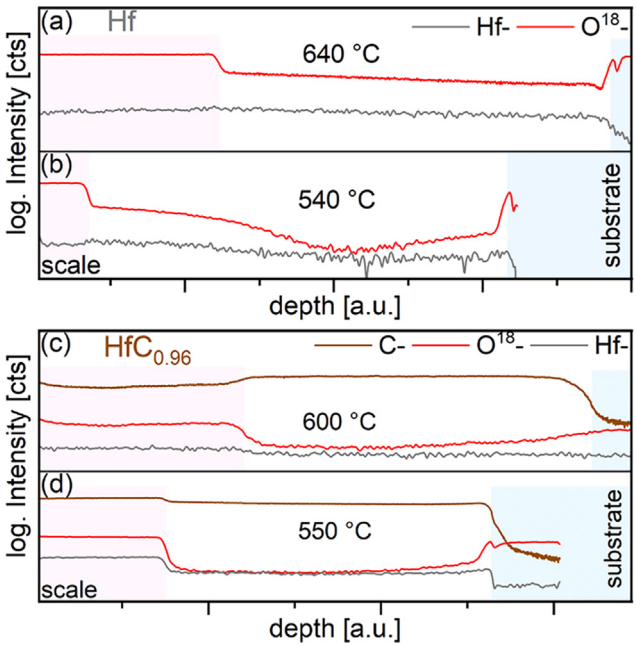

Fig. 5. SIMS analysis of Hf (a-b) and $HfC_{0.96}$ (c-d) coatings after isothermal oxidation at the labelled temperatures. The graphs should be read from left to right in the direction of the SIMS sputter beam, with the surface on the left side and the substrate on the right side.

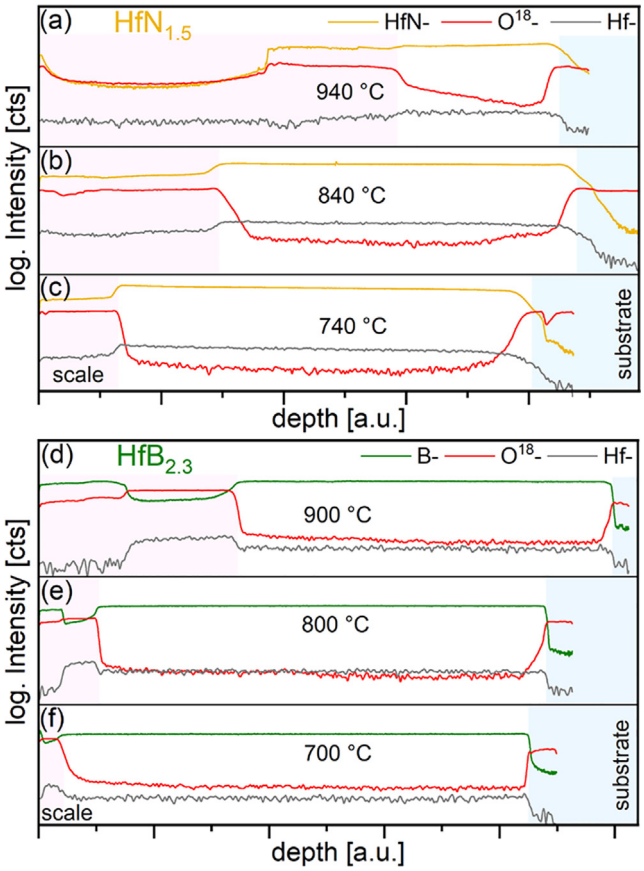

Fig. 6. SIMS analysis of $HfN_{1.5}$ (a-c) and $HfB_{2.3}$ (d-f) coatings after isothermal oxidation at the labelled temperatures. The graphs should be read from left to right in the direction of the SIMS sputter beam, with the surface on the left side and the substrate on the right side.

amounts of carbon detected within the oxide scale. Additional EDX line scans, acquired from a TEM-EDX system, reveal that the carbon and hafnium concentrations in the scale are lower than throughout the remaining coating. Hence, the increased carbon intensity in the scale obtained by SIMS is due to a higher yield of secondary C- and Hf- ions. For 600 °C (Fig. 5c), the scale grows thicker and the coating-substrate interface becomes increasingly blurred, especially for oxygen. Here, also residual oxygen already diffuses through the coating material.

For $HfN_{1.5}$, HfN- ions are used to indirectly trace nitrogen, since the direct detection of nitrogen is very difficult in the negative mode due to the very low yield of N- species. The results in Fig. 6-a-c implicate, that the oxide scale is not completely depleted from nitrogen, but to a certain extent present as a solute. Between 740 °C and 840 °C the O^{18}- intensity profile exhibit a clear drop after the scale suggesting for only slight oxygen diffusion through the remaining coating. However, at 940 °C it intensifies drastically (Fig. 6a). The unsteady signal in the oxide scale at 940 °C is related to surface charging of the already relatively thick oxide scale.

For $HfB_{2.3}$ SIMS data suggests a layered oxide scale formation including a boron and a hafnium rich area (Fig. 6 d-f). Interestingly, at 700 °C the boron enrichment of the scale is absent, whereas above 800 °C this boron rich oxide evolves on the surface. This impression is further supported by SEM cross-sections, where a porous boron oxide layer was observed only above 800 °C. What stands out for $HfB_{2.3}$ is the very low oxygen inward diffusion through the remaining coating. Even at 900 °C (Fig. 6d) there is still a sharp drop of the O^{18}- signal at the scale-coating interface but also at the coating-substrate interface. Hence, the α-HfB_2 structure seems to be a very good diffusion barrier for oxygen.

For all coatings a small Al outward diffusion from the substrate was observed, which follows, except for the Hf coatings, the trend of the O^{18}- signal. For Hf, the Al outward diffusion was much lower than for oxygen.

In Fig. 7, the oxide scale and remaining Hf-coating at 640 °C are depicted. The SEM cross section (Fig. 7a), as well as the TEM bright field (BF) image of the remaining coating, show a typical dense and columnar morphology with a mean column width of 65 nm –

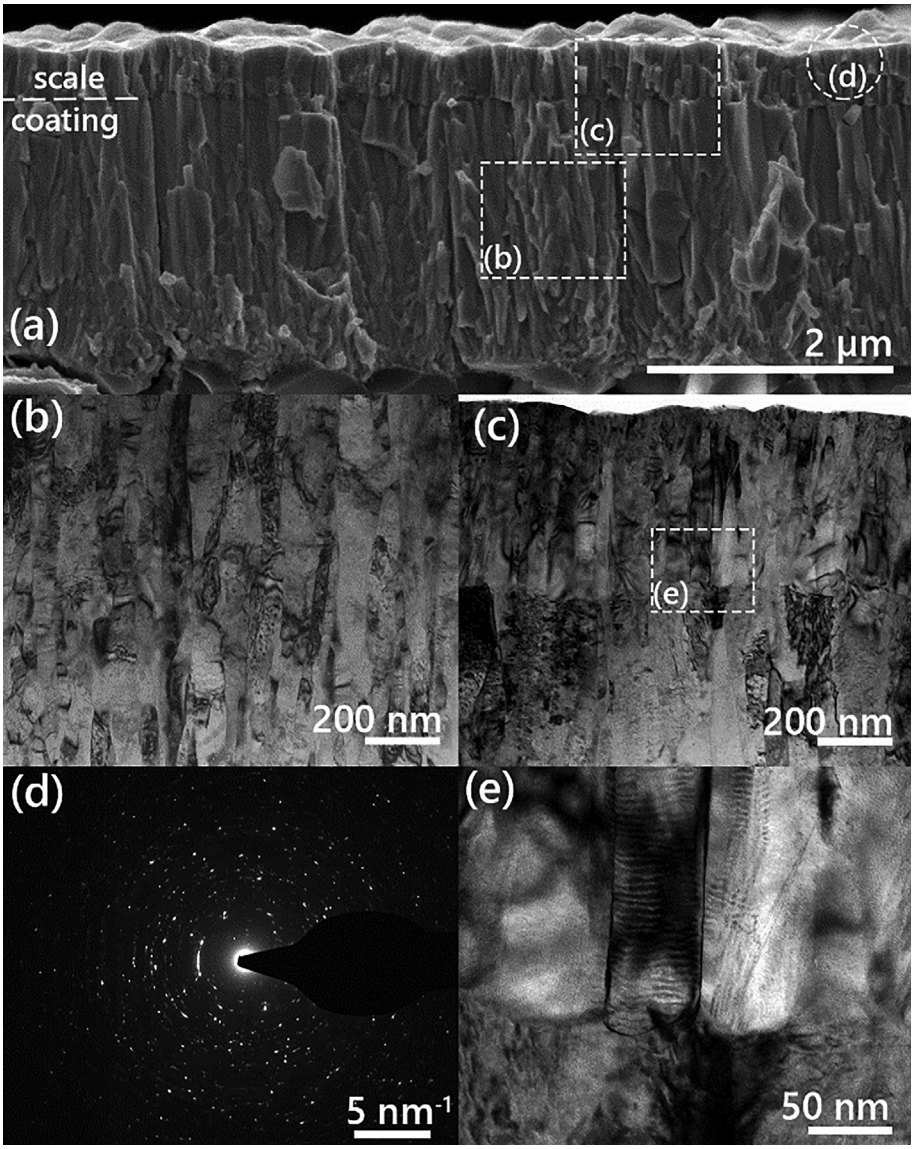

Fig. 7. SEM cross section (a) and TEM images (b-e) of a Hf coating oxidized at 640 °C for 1 h. Bright field images of the remaining coating (b) and the oxide scale (c) show a columnar morphology. The SEAD image (d) confirms the monoclinic structure of the oxide scale which is also observed in XRD. In (e) a magnified image of the Hf-coating/scale interface is shown.

based on TEM dark field (DF) images. Furthermore, the HfO_2 scale on top exhibits a distinct columnar morphology (Fig. 7a, c, and e) with a mean column width of 54 nm. The HfO_2 scale exhibits a thickness of 480 ± 30 nm with a monoclinic crystal structure – also determined by XRD – clearly visible in the SAED image in Fig. 7d (not indexed within the Figure). At 540 °C the scale thickness is 168 ± 20 nm, whereas at 740 °C a 1300 ± 80 nm thick scale could be detected. The magnified image of the scale-coating interface (Fig. 7e) highlights, that the oxide grains do not grow coherently on the metallic Hf columns. However, especially when looking at the SEM cross section or considering the relatively similar column diameters, the impression remains, that the coating and oxide scale morphology are somehow connected. One explanation for this could be the strong oxygen inward diffusion, leading to this high oxygen amounts in the remaining Hf coating. This may prevent a complete re-nucleation at the scale-coating interface.

Fig. 8 shows the oxide scale and remaining $HfC_{0.96}$ coating oxidized at 550 °C. The coating again exhibits a dense columnar structure, however, with a much lower mean columnar width of 31 nm, compared to the Hf coating. What immediately stands out is the amorphous oxide scale, where no grains are visible (Fig. 8c and e) and the SAED only reveals blurred rings being characteristic for an amorphous material (Fig. 8d). The thickness of the oxide scale is 370 ± 35 nm. However, here we have to mention that for HfC the oxide thickness determined on the polycrystalline samples is 100 nm higher than measured on the single crystalline sapphire substrates used for TEM investigations at 550 °C. At 500 °C the scale thickness is 250 ± 20 nm and 580 ± 30 nm at 600 °C (25 min). S. Shimada [37] reported in his study on ZrC, HfC and TiC single crystals different zones at the carbide-oxide interface. In the beginning, incoming oxygen is dissolved in the MeC lattice and forms an oxycarbide $MeC_{1-x}O_x$. The oxygen concentration, x, of this oxycarbide increases until it is saturated. Then dense, pore-free MeO_2 begins to grow parabolically from the MeC lattice – zone 1. When zone 1 achieves a critical thickness the metal oxide starts to crack which is the initiation of zone 2, progressing linearly. However, S. Shimada did not report any amorphous zone, hence the comparison with the $HfC_{0.96}$ coating proves difficult.

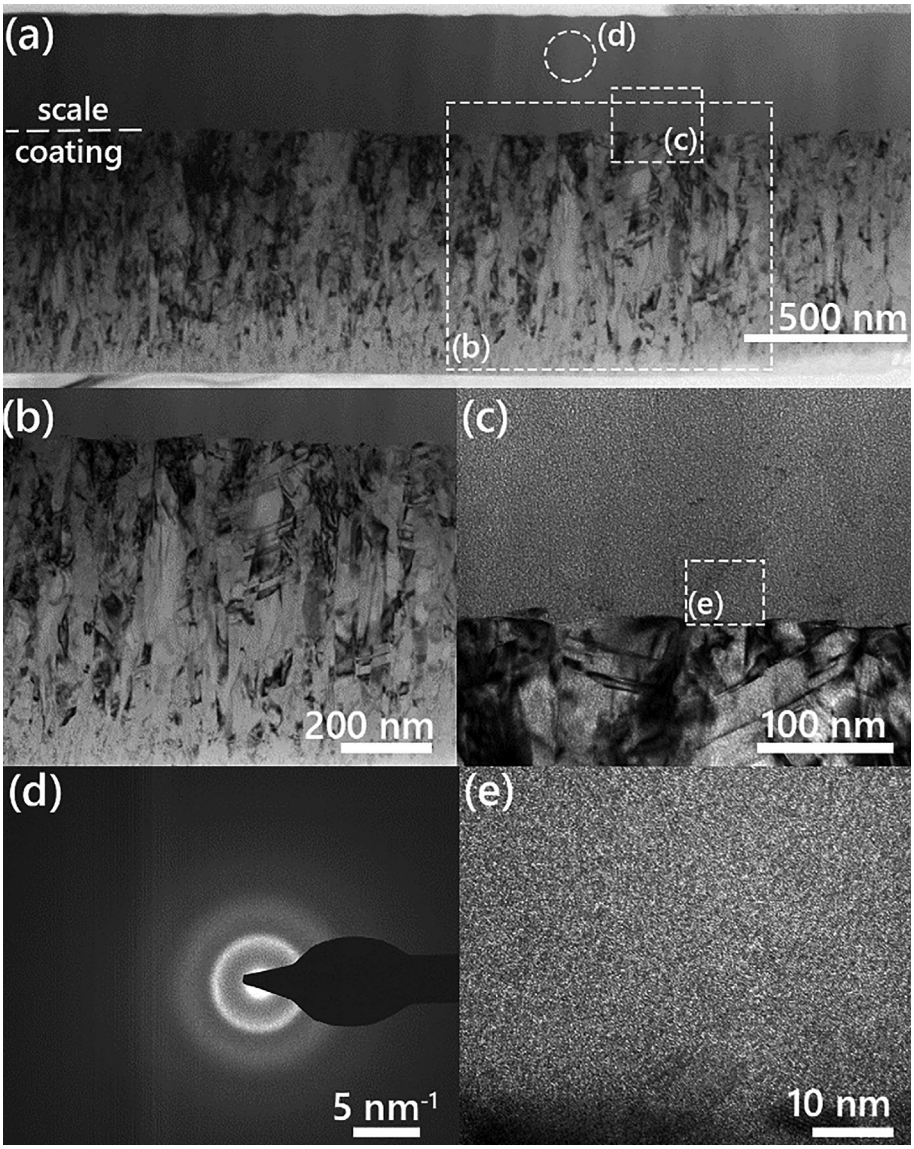

Fig. 8. TEM images of $HfC_{0.96}$ oxidized at 550 °C for 1 h. A BF image of the whole remaining coating and oxide scale is shown in (a) whereas (b) shows a magnified image of the remaining $HfC_{0.96}$ coating and (c) of the oxide scale. No grains are visible in the oxide scale and the SAED image (d) confirms the amorphous appearance. The magnified image of the scale/coating interface shows a rather sharp interface (e).

Along with the SIMS results, it seems that here the oxycarbide and zone 1 are not separated (see Fig. 5c and d), but one amorphous Hf-C-O phase is formed. This is might be connected to the sub-stoichiometry or growth defects (allows higher oxygen solubility). Moreover, the thickness of zone 1 is reported to be between 1 and 2 μm for HfC at 600 °C [37]. Consequently, the $HfC_{0.96}$ coating zone 1 becomes too thick and starts to crack only when the coating is almost completely oxidized. This would explain why also parabolic growth is observed in this study. At 600 °C, however, the growth kinetics transition towards a linear growth behavior and we indeed observed volcano shaped features in the SEM cross sections due to too high stresses and the coating tends to completely spall off the substrate. Furthermore, we would like to mention that at 600 °C the oxide scale still appears amorphous in the XRD spectrum showing no hints of monoclinic HfO_2 as observed for example by Charpentier et al. [38] at higher temperatures (1800 K).

$HfN_{1.5}$ (oxidized at 840 °C) exhibits a dense columnar morphology throughout the remaining unaffected coating (Fig. 9a and b). The oxide scale consists of globular oxide grains with small horizontal cracks (Fig. 9c and e). This globular morphology is also reflected within the SAED image (Fig. 9d), where the individual diffraction spots are more circular, due to the random orientation of the oxide grains when compared to the columnar grains from the oxide formed on top of the Hf coating. The oxide scale thickness is 820 ± 40 nm and the HfO_2, again, exhibits a monoclinic structure. A globular morphology and horizontal cracks are visible for all temperatures, even at 740 °C where the oxide scale thickness was only 330 ± 30 nm. The oxide scale thickness is 460 ± 18 nm at 800 °C (60 min), 819 ± 53 nm at 840 °C (60 min), as well as 1650 ± 50 nm at 940 °C (30 min).

After oxidizing $HfB_{2.3}$ at 900 °C, the remaining coating (Fig. 10a and b) illustrates a very dense and columnar morphology, appearing featureless in the SEM cross section (Fig. 10a). As already mentioned, non-volatile but porous boron oxide forms on top of the surface (above 800 °C), which is suggested to be amorphous due the fact that no peaks indicating the presence of crystalline B_2O_3, were found in the XRD spectra, see Fig. 2d. This porous boron oxide gets very thick (1321 ± 133 nm) at 900 °C and can easily be seen in the SEM cross section (Fig. 10a). The oxide scale can be separated in 2 different zones, the porous region on top (boron rich) and a

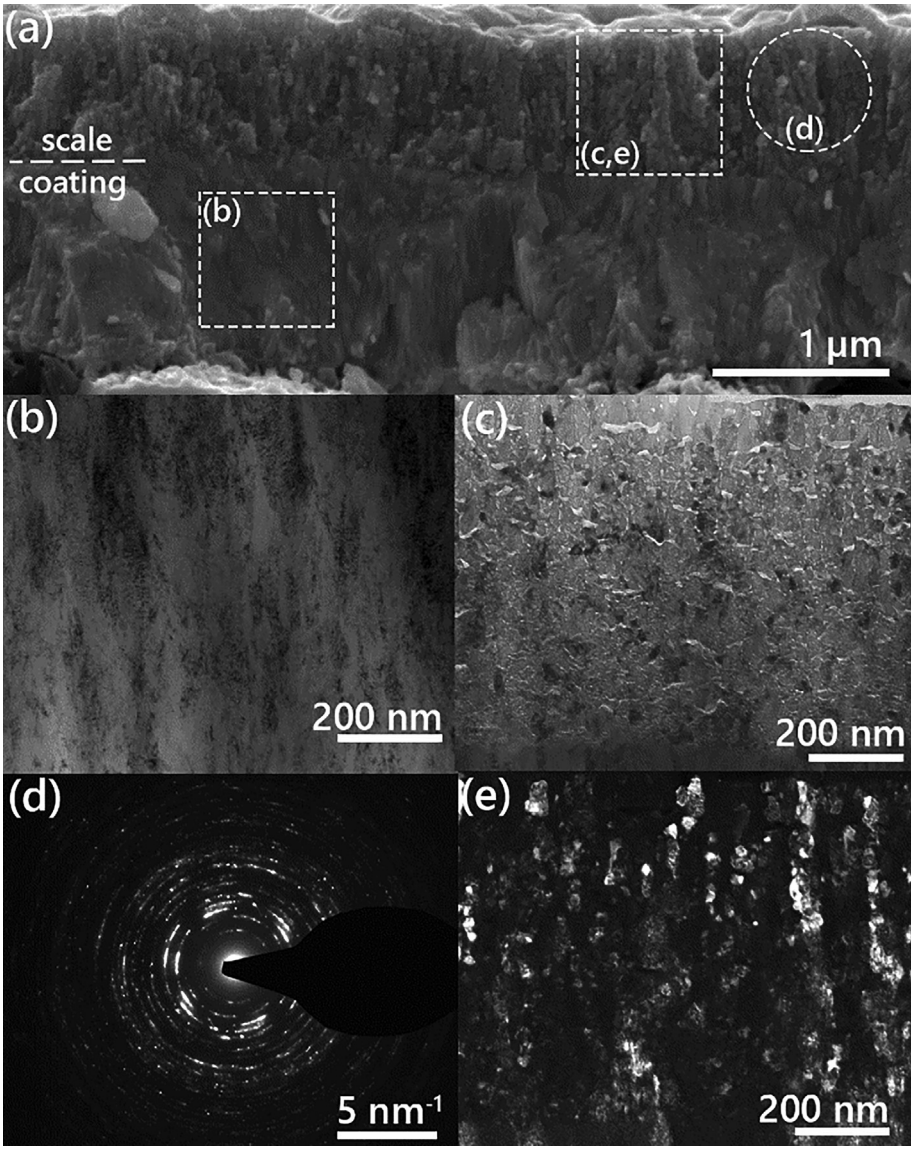

Fig. 9. SEM cross section (a) and TEM images (b-e) of a $HfN_{1.5}$ coating oxidized at 840 °C for 1 h. The remaining coating is shown in (b) and the oxide scale as BF (c) and dark field (DF) image (e). The SAED image (d) confirms the monoclinic structure from XRD and points towards small randomly oriented oxide grains.

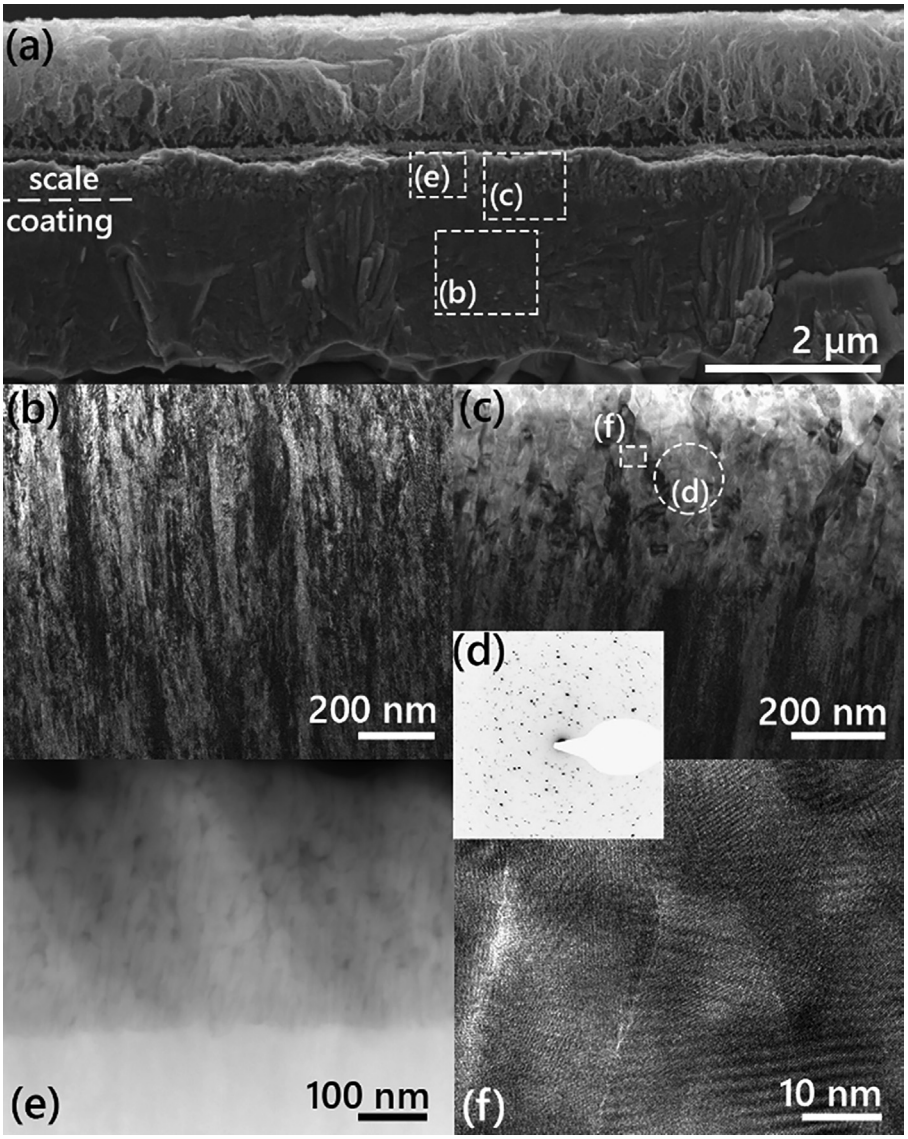

Fig. 10. Oxide scale of $HfB_{2.3}$ oxidized at 900 °C for 30 min. SEM cross section (a) shows the thick porous boron oxide on top and the crystalline oxide below. (b) BF image of the remaining $HfB_{2.3}$ coating and crystalline oxide scale (c). SAED image (d) of the oxide scale shows the monoclinic structure. (e) HAADF image of the oxide scale which shows the Z contrast (bright high Z, dark low Z). (f) HR-TEM image of the oxide scale.

denser, crystalline zone beneath (Hf enriched) – see also Fig. 6d and 10e. The layered oxide structure with B_2O_3 is well reported in various publications, such as for the oxidation of bulk ZrB_2 or HfB_2 [8,39]. On the other hand studies on the oxidation behavior of TM-boride coatings [18,40], done in a conventional furnace in ambient air, do not report any B_2O_3 at the surface. Therefore, we performed comparative oxidation treatments also in a conventional furnace in ambient air confirming this observation. Since B_2O_3 is hygroscopic forming volatile boron acid, the amount of water vapor in the atmosphere has a significant influence on the formation of B_2O_3 [31]. In ambient air a rather high amount of water vapor is present, hence no boron oxide is observed on the surface. In the TG system on the other hand a much lower amount of water vapor is present through the use of synthetic air and the evacuation/He-flushing procedure prior to each oxidation treatment. Therefore, boron oxide remains on the surface. The crystalline HfO_2 below the porous B_2O_3 has a thickness of 460 nm and again exhibits in accordance with XRD a monoclinic structure. For the other oxidation temperatures, the thickness of the crystalline HfO_2 oxide scale is 171 ± 21 nm at 700 °C for 120 min, 182 ± 25 nm at 800 °C for 60 min and 379 ± 51 nm at 840 °C for 60 min. The morphology of the crystalline scale (Fig. 10c) appears similar to the scale on $HfN_{1.5}$, however, with no apparent cracks and less globular grains (more elongated). The STEM-HAADF in Fig. 10e gives the Z contrast in the crystalline scale. One can see that the oxide column boundaries appear dark, indicating that they are rich of an element with low Z. This is in accordance with the model on oxidation of TiB_2, ZrB_2 and HfB_2 presented by Parthasarathy et al. [39] who suggest that the pores between the metal oxide grains are filled with liquid boria. The HR-TEM image (Fig. 10f) again shows these boria rich grain boundaries, appearing bright with a thickness of less than 1 nm. Hence, boria can be found at the grain boundaries, but no pores filled with boria could be identified. Parthasarathy et al. [39] further suggest that at temperatures below ~ 1400 °C, the rate-limiting step is the diffusion of dissolved oxygen through a film of liquid boria in capillaries at the base of the oxidation product.

A sound comparison between $HfN_{1.5}$ and $HfB_{2.3}$ considering the mass gain or oxide scale thickness is not possible due the loss of nitrogen on the one hand, as well as the formation of porous B_2O_3 on the other hand. Hence, we compared how much of the as deposited coating thickness is consumed after oxidation for

60 min. For $HfN_{1.5}$ the as deposited thickness (1.72 μm) is reduced through the oxide scale formation process by 186 ± 30 nm at 800 °C and 487 ± 40 nm at 840 °C, respectively. In comparison, for $HfB_{2.3}$ the as deposited thickness (2.14 μm) decreased by 204 ± 60 nm at 800 °C as well as 491 ± 70 nm at 840 °C. This remarkably similar values therefore suggest, that the HfO_2 formation is the rate limiting step instead of the liquid boria for $HfB_{2.3}$ coatings. To improve the oxidation resistance of HfB_2 the modification of the amorphous boron oxide scale seems to be very interesting and promising. Nevertheless, $HfB_{2.3}$ is a highly dense and efficient coating material to slow down oxygen diffusion at very high temperature.

4. Conclusion

Throughout this study, the influence of the non-metallic species on the oxidation kinetics of Hf-based coatings grown by PVD, Hf, $HfC_{0.96}$, $HfN_{1.5}$, and $HfB_{2.3}$ has been investigated. The different Hf-based compounds exhibit a drastic difference in the oxide scale formation leading to a wide range of respective oxidation onset temperatures. The growth kinetics during isothermal oxidation are all parabolic, except for $HfC_{0.96}$ above 600 °C progressing linearly. The linear change of $\ln(k_p)$ over 1/T with increasing oxidation temperature proves Hf, $HfN_{1.5}$, and $HfB_{2.3}$ to obtain a parabolic growth mode up to 740, 940, and 900 °C, respectively. In addition, the oxygen diffusion through the formed scales is strongly retarded for $HfN_{1.5}$ and $HfB_{2.3}$ e.g. exhibiting k_p values of $5.66 \cdot 10^{-11}$ and $4.97 \cdot 10^{-10}$ $kg^2m^{-4}s^{-1}$ at 840 °C. Nevertheless, comparing these outstanding low k_p values, the loss of N next to the formation of B_2O_3 needs to be considered. In contrast, within the metallic Hf coatings the oxygen inward diffusion is predominant, progressing down to the coating-substrate interfaces beneath the columnar HfO_2 scale. $HfC_{0.96}$ exhibits also an ineffective, amorphous oxycarbide scale, being not as protective compared to the other coating materials. $HfN_{1.5}$ exhibits a distinct HfO_2 scale with a globular morphology and small horizontal cracks throughout the scale. As mentioned above the growth kinetic is significantly retarded, also compared to the metallic Hf coating, obtaining similar kinetic constants such as Cr_2O_3 growing on Cr. $HfB_{2.3}$ exhibits a layered scale with an amorphous but porous B_2O_3 on top of the surface followed by a dense and crystalline HfO_2 below. In addition, $HfB_{2.3}$ stands out due to its super high hardness of 47.7 ± 2.7 GPa, and exceptional low oxygen inward diffusion during oxidation. Comparing the remaining unoxidized regions for $HfN_{1.5}$ and $HfB_{2.3}$ at 800 and 840 °C, the consumed thicknesses is about 200 and 490 nm, respectively. Our results clearly reveal the strong influence of the non-metal species on the oxidation resistance of Hf-based coating materials. Furthermore, the formation of an adherent and highly effective layered scale on top of $HfB_{2.3}$ suggest for a great potential with respect to oxidation resistance at extreme conditions.

Data availability

The data that support the findings of this study are available from the corresponding author upon reasonable request.

Declaration of Competing Interest

The authors declare that they have no known competing financial interests or personal relationships that could have appeared to influence the work reported in this paper.

Acknowledgment

The financial support by the Austrian Federal Ministry for Digital and Economic Affairs, the National Foundation for Research, Technology and Development and the Christian Doppler Research Association is gratefully acknowledged (Christian Doppler Laboratory "Surface Engineering of high-performance Components"). We also thank for the financial support of Plansee SE, Plansee Composite Materials GmbH, and Oerlikon Balzers, Oerlikon Surface Solutions AG. In addition, we want to thank the X-ray center (XRC) of TU Wien for beam time as well as the electron microscopy center - USTEM TU Wien - for using the SEM and TEM facilities. The authors acknowledge TU Wien Bibliothek for financial support through its Open Access Funding Programme. Support by VR-RFI (#2017-00646_9 & 2019-00191) and the Swedish Foundation for Strategic Research (SSF, contract RIF14-0053) supporting accelerator operation is gratefully acknowledged.

Appendix

Table A1.

Table A1
Elemental compositions of the coatings determined by ERDA/EBS, respectively.

Label	**Hf** (at.%)	**Zr** (at.%)	**C** (at.%)	**N** (at.%)	**B** (at.%)	**O** (at.%)
Hf	93.5/93	6.4/7				0.1
$HfC_{0.96}$	46.9/48.0	1.4/1.5	47.8/46.5			3.9/4.0
$HfN_{1.5}$	36.5/36.3	3.6/3.5		59.8/60.2		0.1
$HfB_{2.3}$	29.8/30				70.2/70	–

References

[1] V. Kumar, K. Balasubramanian, Progress update on failure mechanisms of advanced thermal barrier coatings: A review, Prog. Org. Coat. 90 (2016) 54–82.
[2] Y. Tamarin, Protective coatings for turbine blades, (2002). https://books.google.at/books?hl=en&lr=&id=LB9eItW_7CUC&oi=fnd&pg=PR5&dq=.Tamarin, ProtectiveCoatingsforTurbineblades,ASMInternational,MaterialsPark, Ohio,2002.&ots=s5uSzABzJZ&sig=ZK99gpYBZzlzxFrOobrg2uQwDco.
[3] J.H. Perepezko, The hotter the engine, the better, Science. 326 (5956) (2009) 1068–1069.
[4] J. Ast, Z. Balogh-Michels, M. Döbeli, A. Dommann, M. Gindrat, X. Maeder, A. Neels, M.N. Polyakov, H. Rudigier, B. Widrig, J. Ramm, The formation of a homogeneous α-alumina coating on a Ni-based superalloy from a layer stack deposited by cathodic arc evaporation, Surf. Coat. Technol. 360 (2019) 329–334.
[5] W. Münz, Titanium aluminum nitride films: A new alternative to TiN coatings, J. Vac. Sci. Technol. A. 4 (1986) 2717–2725.
[6] E. Wuchina, E. Opila, M. Opeka, W. Fahrenholtz, I. Talmy, UHTCs: ultra-high temperature ceramic materials for extreme environment applications, Electrochem. Soc. Interface. 16 (2007) 30.
[7] W.G. Fahrenholtz, E.J. Wuchina, W.E. Lee, Y. Zhou, Ultra-High Temperature Ceramics, John Wiley & Sons Inc, Hoboken, NJ, 2014.
[8] W.G. Fahrenholtz, G.E. Hilmas, Oxidation of ultra-high temperature transition metal diboride ceramics, Int. Mater. Rev. 57 (1) (2012) 61–72.
[9] P.H. Mayrhofer, R. Rachbauer, D. Holec, F. Rovere, J.M. Schneider, 4.14 - Protective Transition Metal Nitride Coatings, in: S.H.F.B.J.V.T. Yilbas (Ed.), Compr. Mater. Process., Elsevier, Oxford, 2014: pp. 355–388.
[10] L. Chen, J. Paulitsch, Y. Du, P.H. Mayrhofer, Thermal stability and oxidation resistance of Ti–Al–N coatings, Surf. Coat, Technol, 2012. https://www.sciencedirect.com/science/article/pii/S0257897211012382.
[11] R. Hollerweger, H. Riedl, J. Paulitsch, M. Arndt, R. Rachbauer, P. Polcik, S. Primig, P.H. Mayrhofer, Origin of high temperature oxidation resistance of Ti–Al–Ta–N coatings, Surf. Coat. Technol. 257 (2014) 78–86.
[12] G. Greczynski, B. Bakhit, L. Hultman, M. Odén, High Si content TiSiN films with superior oxidation resistance, Surf. Coat. Technol. 398 (2020) 126087.
[13] M. to Baben, M. Hans, D. Primetzhofer, S. Evertz, H. Ruess, J.M. Schneider, Unprecedented thermal stability of inherently metastable titanium aluminum nitride by point defect engineering, Materials Research Letters. 5 (3) (2017) 158–169.
[14] I.C. Schramm, M.P. Johansson Jõesaar, J. Jensen, F. Mücklich, M. Odén, Impact of nitrogen vacancies on the high temperature behavior of (Ti1−xAlx)Ny alloys, Acta Mater. 119 (2016) 218–228.
[15] I.n. S. Choi, J. C. Park, The corrosion behavior of TiAlN coatings prepared by PVD in a hydrofluoric gas atmosphere, Surf. Coat. Technol. 131 (1-3) (2000) 383–385.
[16] V. Moraes, H. Riedl, C. Fuger, P. Polcik, H. Bolvardi, D. Holec, P.H. Mayrhofer, Ab initio inspired design of ternary boride thin films, Sci. Rep. 8 (2018) 9288.
[17] H. Riedl, T. Glechner, T. Wojcik, N. Koutná, S. Kolozsvári, V. Paneta, D. Holec, D. Primetzhofer, P.H. Mayrhofer, Influence of carbon deficiency on phase formation and thermal stability of super-hard TaCy thin films, Scr. Mater. 149 (2018) 150–154.

[18] B. Bakhit, J. Palisaitis, J. Thörnberg, J. Rosen, P.O.Å. Persson, L. Hultman, I. Petrov, J.E. Greene, G. Greczynski, Improving the high-temperature oxidation resistance of TiB2 thin films by alloying with Al, Acta Mater. 196 (2020) 677–689.
[19] B. Bakhit, S. Dorri, A. Kooijman, Z. Wu, J. Lu, J. Rosen, J.M.C. Mol, L. Hultman, I. Petrov, J.E. Greene, G. Greczynski, Multifunctional ZrB2-rich Zr1-xCrxBy thin films with enhanced mechanical, oxidation, and corrosion properties, Vacuum. 185 (2021) 109990.
[20] T. Massalski, P.R. Subramanian, Hf (Hafnium) Binary Alloy Phase Diagrams, ASM international Cleveland (1990).
[21] K. Balasubramanian, S.V. Khare, D. Gall, Valence electron concentration as an indicator for mechanical properties in rocksalt structure nitrides, carbides and carbonitrides, Acta Mater. 152 (2018) 175–185.
[22] S.F. Pugh, XCII. Relations between the elastic moduli and the plastic properties of polycrystalline pure metals, The London, Edinburgh, and Dublin Philosophical Magazine and Journal of Science. 45 (1954) 823–843.
[23] P. Ström, P. Petersson, M. Rubel, G. Possnert, A combined segmented anode gas ionization chamber and time-of-flight detector for heavy ion elastic recoil detection analysis, Rev. Sci. Instrum. 87 (2016) 103303.
[24] J.A. Leavitt, L.C. McIntyre, M.D. Ashbaugh, J.G. Oder, Z. Lin, B. Dezfouly-Arjomandy, Cross sections for 170.5° backscattering of 4He from oxygen for 4He energies between 1.8 and 5.0 MeV, Nucl. Instrum. Methods Phys. Res. B. 44 (3) (1990) 260–265.
[25] C.-K. Lee, E. Cho, H.-S. Lee, C.S. Hwang, S. Han, First-principles study on doping and phase stability of HfO_2, Phys. Rev. B Condens. Matter. 78 (2008) 012102.
[26] Dongwon Shin, Raymundo Arróyave, Zi-Kui Liu, Thermodynamic modeling of the Hf–Si–O system, CALPHAD. 30 (4) (2006) 375–386.
[27] M.M. Opeka, I.G. Talmy, J.A. Zaykoski, Oxidation-based materials selection for 2000°C + hypersonic aerosurfaces: Theoretical considerations and historical experience, J. Mater. Sci. 39 (2004) 5887–5904.
[28] W.M. Haynes, CRC Handbook of Chemistry and Physics, 93rd Edition., CRC Press LLC, Baton Rouge, 2012.
[29] S. Shimada, A thermoanalytical study on the oxidation of ZrC and HfC powders with formation of carbon, Solid State Ionics. 149 (2002) 319–326.
[30] William G. Fahrenholtz, Gregory E. Hilmas, Inna G. Talmy, James A. Zaykoski, Refractory Diborides of Zirconium and Hafnium, J. Am. Ceram. Soc. 90 (5) (2007) 1347–1364.
[31] Ravisankar Naraparaju, Keyur Maniya, Alec Murchie, William G. Fahrenholtz, Gregory E. Hilmas, Effect of moisture on the oxidation behavior of ZrB2, J. Am. Ceram. Soc. 104 (2) (2021) 1058–1066.
[32] T. Glechner, S. Lang, R. Hahn, M. Alfreider, V. Moraes, D. Primetzhofer, J. Ramm, S. Kolozsvári, D. Kiener, H. Riedl, Correlation between fracture characteristics and valence electron concentration of sputtered Hf-C-N based thin films, Surf. Coat. Technol. 399 (2020) 126212.
[33] Ralf Bürgel, Hans Jürgen Maier, Thomas Niendorf (Eds.), Handbuch Hochtemperatur- Werkstofftechnik, Vieweg+Teubner, Wiesbaden, 2011.
[34] P. Kofstad, High-temperature oxidation of metals(Book on high temperature oxidation of metals and alloys, fundamental aspects and reaction mechanisms), NEW YORK, JOHN WILEY AND SONS, INC. , 1966. 352 P. (1966).
[35] Neil Birks, Gerald H. Meier, Frederick S. Pettit (Eds.), Introduction to the High-Temperature Oxidation of Metals, Cambridge University Press, Cambridge, 2006.
[36] E. Aschauer, T. Wojcik, P. Polcik, O. Hunold, M. Arndt, V. Dalbauer, P.H. Mayrhofer, P. Felfer, H. Riedl, Ultra-high oxidation resistance of nano-structured thin films, Mater. Des. 201 (2021) 109499.
[37] Shiro SHIMADA, Oxidation and mechanism of single crystal carbides with formation of carbonカーボン生成を伴う単結晶炭化物の酸化と機構, J. Ceram. Soc. Jpn. 109 (1267) (2001) S33–S42.
[38] Ludovic Charpentier, Marianne Balat-Pichelin, Jean-Louis Sans, Diletta Sciti, Laura Silvestroni, Effect of high temperature oxidation on the radiative properties of HfC-based ceramics, Corros. Sci. 126 (2017) 255–264.
[39] T.A. Parthasarathy, R.A. Rapp, M. Opeka, R.J. Kerans, A model for the oxidation of ZrB2, HfB2 and TiB2, Acta Mater. 55 (17) (2007) 5999–6010.
[40] C. Fuger, B. Schwartz, T. Wojcik, V. Moraes, M. Weiss, A. Limbeck, C.A. Macauley, O. Hunold, P. Polcik, D. Primetzhofer, P. Felfer, P.H. Mayrhofer, H. Riedl, Influence of Ta on the oxidation resistance of WB2−z coatings, J. Alloys Compd. 864 (2021) 158121, https://doi.org/10.1016/j.jallcom.2020.158121.
[41] International Center of Diffraction Data, Powder diffraction file 00-005-0670, (2019).
[42] International Center of Diffraction Data, Powder diffraction file 04-003-6121, (2019).
[43] International Center of Diffraction Data, Powder diffraction file 04-002-0653, (2019).
[44] International Center of Diffraction Data, Powder diffraction file 04-002-0174, (2019).
[45] International Center of Diffraction Data, Powder diffraction file 04-004-3850, (2019).
[46] International Center of Diffraction Data, Powder diffraction file 04-010-6477, (2019).